Comparison of the ASI Ice Concentration Algorithm With Landsat-7 ETM+ and SAR Imagery

Heidrun Wiebe, Georg Heygster, *Member, IEEE*, and Thorsten Markus, *Member, IEEE*

Abstract—Continuous monitoring of sea ice and its changes is mainly done by passive microwave sensors on satellites. One frequently used technique of retrieving sea-ice concentrations is the Arctic Radiation and Turbulence Interaction STudy Sea Ice (ASI) algorithm, which uses the near-90-GHz channels, here those of the Advanced Microwave Scanning Radiometer—Earth Observing System to calculate sea-ice concentrations. The ASI ice concentrations are compared with ice concentrations derived from the following: 1) the multispectral imager Enhanced Thematic Mapper Plus operating on Landsat and 2) from Envisat and Radarsat SAR images. In this paper, we focus on marginal ice zones, as the ice concentrations in those regions are in general observed with higher errors. First-year ice (bias: -1%–0% and rms error: 1%–4%) and young ice (bias: -4%–0% and rms error: 3%–9%) are fairly well recognized with little underestimation of ASI ice concentrations with respect to Landsat ice concentrations. New ice is identified with less accuracy by the ASI algorithm (bias: -16%–9% and rms error: 18.3%–26.2%). Averaged over all ice types, the bias ranges between -8.4% and 4.5%, and the rms error ranges between 2.0% and 17.4%. Discrepancies mainly occur in polynya areas (underestimation by ASI) and along the ice edge (overestimation by ASI). The results of the ASI–SAR comparison yield contrasting results. ASI underestimates the ice concentrations near the ice edge but overestimates them in some interior areas (bias: -2.9%–2.5% and rms error: 16.9%–20.1%). The discrepancies between both comparisons may be due to the different interaction mechanisms of the different sensor types, particularly with the newly formed ice.

Index Terms—Remote sensing, sea ice.

I. INTRODUCTION

RETRIEVAL of sea-ice concentrations is mainly based on passive microwave observations, because this technique also works at night and under cloudy conditions. The ASI algorithm uses the near-90-GHz channels of the Special Sensor Microwave/Imager and the Advanced Microwave Scanning Radiometer—Earth Observing System (AMSR-E), which have a higher spatial resolution than the lower frequency channels (up to 36 GHz). The high spatial resolution of 5 km distinguishes the ASI results from those of other ice concentration algorithms such as the NASA Team [1], [2] or bootstrap [3], [4] or algorithms, which use the lower frequency channels and have a spatial resolution of about 25 km.

So far, the ASI ice concentrations have only been compared with other ice concentration algorithms that also use passive microwave data and to visual observations during two ship cruises on the RV Polarstern [5]. In this paper, we compare the ASI ice concentrations with ice concentrations derived from optical and SAR data. In order to assess the ASI ice concentrations, we need an independent and reliable comparison source. Here, we use optical data from the multispectral imager Enhanced Thematic Mapper Plus (ETM+) operating on Landsat-7. The method to derive ice concentrations from these data is based on the albedo difference between open water and various sea-ice types and has been used in a similar comparison study by Cavalieri *et al.* [6] for the NASA Team 2 (NT2) algorithm [7]. We kept our comparison similar to the NT2 study using the same validation data and method for compatibility, so the results can therefore be easily compared. The comparison with optical data can only be performed with clear-sky cases, so we additionally include a comparison with SAR data, which allows us to have larger areas of high-resolution sea-ice observations in cloudy situations. Because of the varying contrast between open water and sea ice in SAR scenes, it is not trivial to determine ice concentrations from them. Here, we use the method by Bøvith and Andersen [8] to derive ice concentrations from single-polarized SAR images, based on supervised neural-network classification of second-order gray-level statistical features.

Although we only have few scenes for the comparisons, it can give us useful hints about strengths and weaknesses of the performance of the ASI algorithm. In the ice interior where the ice concentrations are almost 100%, we do not expect large errors. Therefore, we selected scenes in the marginal ice zones, which consist of new, young, and first-year ice.

II. DATA SETS

The data used in this comparison are the ASI data set (Section II-B) and the Landsat data set (Section II-A). The two data sets are described, and the method to colocate and match the resolution of the different data sets is explained (Section II-C). In the ASI data set, the tie points are adapted toward the Landsat data set (Section II-D). The SAR data set is described separately in Section IV-A.

A. Landsat

The Landsat ETM+ images were acquired during March 2003 in the area of the Bering Sea and the Bering Strait (Fig. 1).
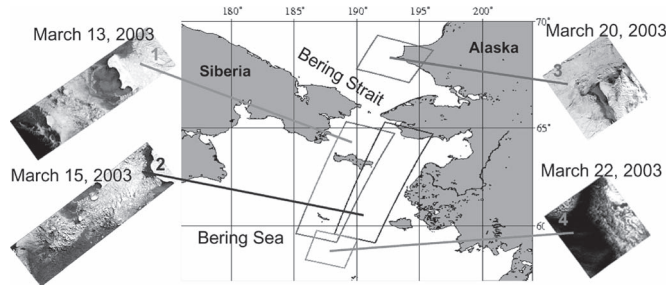
Fig. 1. Locations of the four Landsat scenes in the Bering Sea.

The four scenes cover various ice conditions (e.g., ice edges, polynyas, and closed ice cover) and ice types (new, young, and first-year ice), having mostly clear-sky conditions.

The physical quantity of the data is the albedo ρ (herein, the ETM+-derived "albedo" refers to a broadband top-of-the-atmosphere albedo in the 0.52–0.90-μm range), which is calculated from the spectral radiance of the panchromatic band (0.52–0.9 μm) of the ETM+ by [9]

$$\rho = \frac{\pi L_\lambda d^2}{ESUN_\lambda \cos \theta_s}$$

where L_λ is the spectral radiance at the sensor's aperture, d is the Earth–Sun distance in astronomical units, $ESUN_\lambda$ denotes the mean exoatmospheric irradiances, and θ_s is the solar zenith angle in degrees. The data are gridded to a polar-stereographic grid with a grid size of 150 m.

B. ASI

The ASI data set is calculated based on the ASI ice concentration algorithm, using AMSR-E Level 1A data gridded to a 6.25-km polar-stereographic grid. The ASI algorithm is based on the polarization differences between vertically and horizontally polarized radiation at 89 GHz. Two tie points are defined, namely, the polarization difference P_0 for open water, i.e., where the ice concentration is 0%, and P_1 for 100% ice concentration. These are obtained by comparison with well-validated reference data (e.g., from the NASA Team or bootstrap algorithm). Ice concentrations between 0% and 100% are retrieved by interpolation using a third-order polynomial

$$C = d_3 P^3 + d_2 P^2 + d_1 P + d_0 \qquad (1)$$

where C is the ice concentration, P is the polarization difference, and d_0–d_3 are constant coefficients computed from the tie points P_0 and P_1. More details on the ASI algorithm are found in [5] and [10]. In this comparison, the grid size of 12.5 km is chosen in order to easily compare the results with those of Cavalieri *et al.* [6]. Additionally, only data of the swath with the lowest time difference to the Landsat data set are used in order to minimize the time difference between the data sets.

C. Mapping Landsat Albedo to Ice Concentration

Comparing different Earth observation data sets requires a colocation and a resolution matching. In the ASI data set, we have ice concentrations on a 12.5-km grid, while in the Landsat

data set, we have albedos on a 150-m grid. Both grids are polar stereographic. The mapping of the Landsat albedos to ice concentrations on the ASI grid is done by a threshold method, which was also used in [6]. It consists of two steps.

1) An ice–water albedo threshold of 0.1 is applied to the Landsat data, setting all Landsat pixels with albedo below 0.1 to 0% IC and all above 0.1 to 100% IC.
2) The Gaussian weighted mean is taken from the Landsat pixels within a neighborhood of 83×83 pixels. This is how many times the Landsat footprint of 150-m diameter fits into one ASI pixel of 12.5-km diameter.

D. ASI Tie-Point Adaptation

After mapping the Landsat albedos to ice concentrations on the ASI grid (Section II-C), the ASI tie points P_0 and P_1 are adapted toward the Landsat ice concentrations. The adaptation method is given by Spreen *et al.* [5]. It uses the iterative simplex method by Nelder and Mead [11] that minimizes a selectable parameter (here, the rms of the differences between the data sets) by varying the two free variables (here, the two tie points) and taking as optimal values those where the rms difference is at the minimum. The step size adjusts from large values in the beginning to smaller ones at the end when getting close to the minimum. The adaptation of ASI toward Landsat was done for the scenes that included water pixels: *Scene 1* and *Scene 4* (Fig. 1). The resulting optimal tie points are $P_0 = 81.3$ K and $P_1 = 24.1$ K for *Scene 1* and $P_0 = 72.1$ K and $P_1 = 12.8$ K for *Scene 4*. Because the number of pixels in *Scene 1* is 3.5 times larger than that in *Scene 4*, we select the tie points to be closer to the optimal tie points of *Scene 1*, roughly rounded to $P_0 = 80$ K and $P_1 = 20$ K. The polynomials of the tie points selected here and the operational ASI tie points (used for the daily ASI ice maps) are shown in Fig. 2, together with the polarization difference of the data points related to the Landsat ice concentration. We use the Landsat-adapted tie points ($P_0 = 80$ K and $P_1 = 20$ K) in order to have a bias of ice concentrations between ASI and Landsat that is close to 0%. For instance, with the operational tie points ($P_0 = 47$ K and $P_1 = 11.7$ K), which are used for our daily computed ASI ice maps, there was a large negative bias, as all pixels in the polynya south of St. Lawrence Island were recognized as open water. When we compared the ASI ice concentrations (using the Landsat-adapted tie points) with the SAR ice concentrations, the bias was also close to 0%. As both comparison data are independent of each other, we consider the tie points chosen here also as independent. More discussion on the tie points is given in Section III-C.

III. COMPARISON: ASI–LANDSAT ICE CONCENTRATIONS

The results of the four different Landsat scenes were very similar, so we only present a detailed analysis of *Scene 1*. The details on all four scenes are found in Table I. The first column has the areal and temporal details about the different scenes, the second column gives the mean and standard deviation of ice concentrations derived from the Landsat data (excluding water),
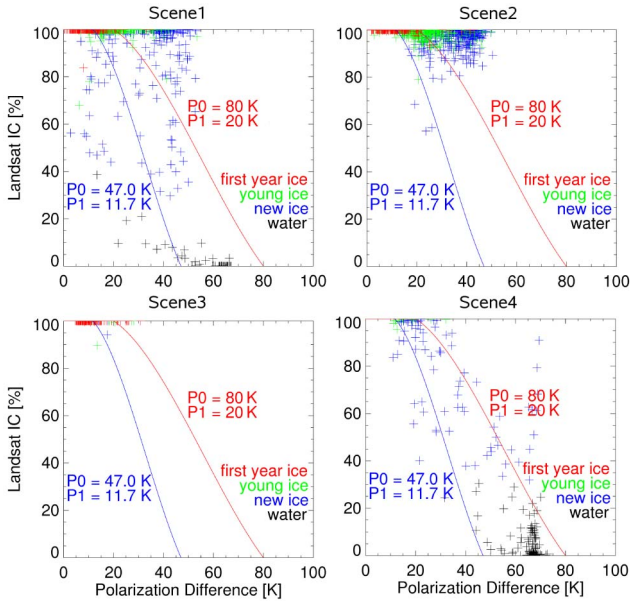
Fig. 2. Landsat ice concentrations related to polarization differences P's for all four scenes. Third-order polynomials of (red curve) Landsat-adapted tie points and (blue curve) operational ASI tie points are overlaid.

and the third and fourth columns show the bias and rms error of the Landsat–ASI and the Landsat–NT2 comparison.

In addition to ice concentrations, the scenes are also analyzed for different ice types classified according to their albedo in the Landsat imagery: Pixels with values below the albedo of 0.1 are classified as water, from 0.1 to 0.4 as new ice, from 0.4 to 0.6 as young ice, and above 0.6 as first-year ice. The values for the thresholds are taken from Cavalieri *et al.* [6]. These values are somewhat different to direct surface albedo measurements because the top-of-the-atmosphere albedos tend to be slightly higher than the actual surface albedo [12].

A. Scene 1: March 13, 2003

The results of the comparison of Landsat *Scene 1* are shown in Fig. 3(a)–(d). It shows maps of the ice concentrations of ASI [Fig. 3(a)] and Landsat [Fig. 3(b)], their differences [Fig. 3(c)], and the ice-type classification [Fig. 3(d)]. The image of the ice concentration differences between ASI and Landsat shows that ASI underestimates the ice concentrations in an area south of St. Lawrence Island (blue) but overestimates them along the ice edge (red). From the ice-type image, we see that we have a large refrozen polynya south of St. Lawrence Island, which is indicated by the new ice. Polynyas are areas of open water within the ice, formed by wind forcing or raising of warm-water masses. Those areas may refreeze again, resulting in an area of new ice surrounded by older ice. The St. Lawrence Island polynya is a persistent polynya formed by strong northern and eastern winds, pushing the ice away from the coast [13].

The correlation of ice concentrations IC_{ASI} versus $IC_{Landsat}$ is shown in the scatter plot of Fig. 3(e). Pixels are classified by ice types and open water, according to the averaged albedo over those Landsat pixels that correspond to one ASI pixel. At first hand, we see a large scatter of new ice, which generally has lower Landsat ice concentrations

than young and first-year ice. Most of the new ice pixels are located below the diagonal at the right edge of the scatter plot. They mostly stem from the polynya area where ASI underestimates the ice concentration. There are some pixels above the diagonal, referring to the overestimation of IC_{ASI} at the ice edge. Altogether, we have a negative bias of -10.4% and an rms error of 26.2% for new ice. Young ice and first-year ice have a much better agreement between IC_{ASI} and $IC_{Landsat}$. The pixels are mainly located near the upper right corner of the scatter plot. The biases (young ice: -2.6% and first-year ice: -0.2%) and rms errors (young ice: 7.4% and first-year ice: 1.2%) are much lower than that for new ice and open water. The latter has a large positive bias of 16.9% and an rms error of 31.7%. These errors arise along the ice edge, and IC_{ASI} already sees ice where $IC_{Landsat}$ still recognizes water. It means that the IC_{ASI} ice edge is shifted toward the open water, relative to the $IC_{Landsat}$ ice edge. Summarizing all surface types gives a bias of -3.5% and an rms error of 17.4%.

B. Summary of All Scenes and Comparison With Previous Study

The distribution statistics of ice concentrations of the Landsat data is given in Table I. The mean ice concentration is highest for Scene 3 (almost 100%) where mainly first-year ice is present. In Scenes 1 and 2, it is slightly lower (96%–97%), as there is also young and new ice present. In Scene 4, it is quite low (72%), as there is only young and new ice present. Ice concentration distribution is rather homogeneous in Scenes 2 and 3 (low standard deviation of 1%–4%), whereas in Scenes 1 and 4, there is a larger range of ice concentrations (standard deviation of 11%–32%).

The results of the biases and rms errors of all four scenes are summarized in Fig. 3(f), together with the pixel-weighted average of all four scenes. It reveals that ASI can detect first-year ice and young ice fairly well, with little underestimation of ice concentrations. The high errors of open water in *Scene 1* contribute only little to the overall rms error of open-water pixels, as there are less open-water pixels in *Scene 1* (41) than in *Scene 4* (102). In general, the ASI algorithm overestimates the sea ice near the ice edge. The surface type causing the highest errors is the new ice with rms values between 18.3% and 26.2%. The bias is lowest (-16.4%) in *Scene 2* where we have only the polynya, it is highest (8.5%) in *Scene 4* where we have only the ice edge, and it is a bit higher in *Scene 1* (-10.4%) than in *Scene 2* where we have both polynya and ice edge, whereas the polynya area is larger than the ice-edge area.

The comparison of NT2-versus-Landsat ice concentrations by Cavalieri *et al.* [6] did show little underestimation of ice concentrations (bias: -1.9%) by the NT2 algorithm, except for *Scene 4*, which had a bias of -13.8% (Table I). The rms errors lie between 1.2% and 6.6% for *Scenes 1–3*, and 15.8% for *Scene 4*. The large bias and rms error of *Scene 4* are explained by substantial changes in ice concentrations during the 2-h time difference between the AMSR-E and the Landsat observation, mainly associated with the production of new ice, specifically in the diffuse marginal ice zones. Regarding different ice types, the rms error for first-year ice is 1.2%–4.7%; for young ice,

TABLE I

DETAILS OF THE FOUR LANDSAT SCENES AND COMPARISON OF THE ICE CONCENTRATIONS WITH THOSE FROM THE ASI AND
THE NT2 ALGORITHM. T IS THE ACQUISITION TIME IN UTC. ETM+ IS THE ICE CONCENTRATION OF THE ETM+ SCENE

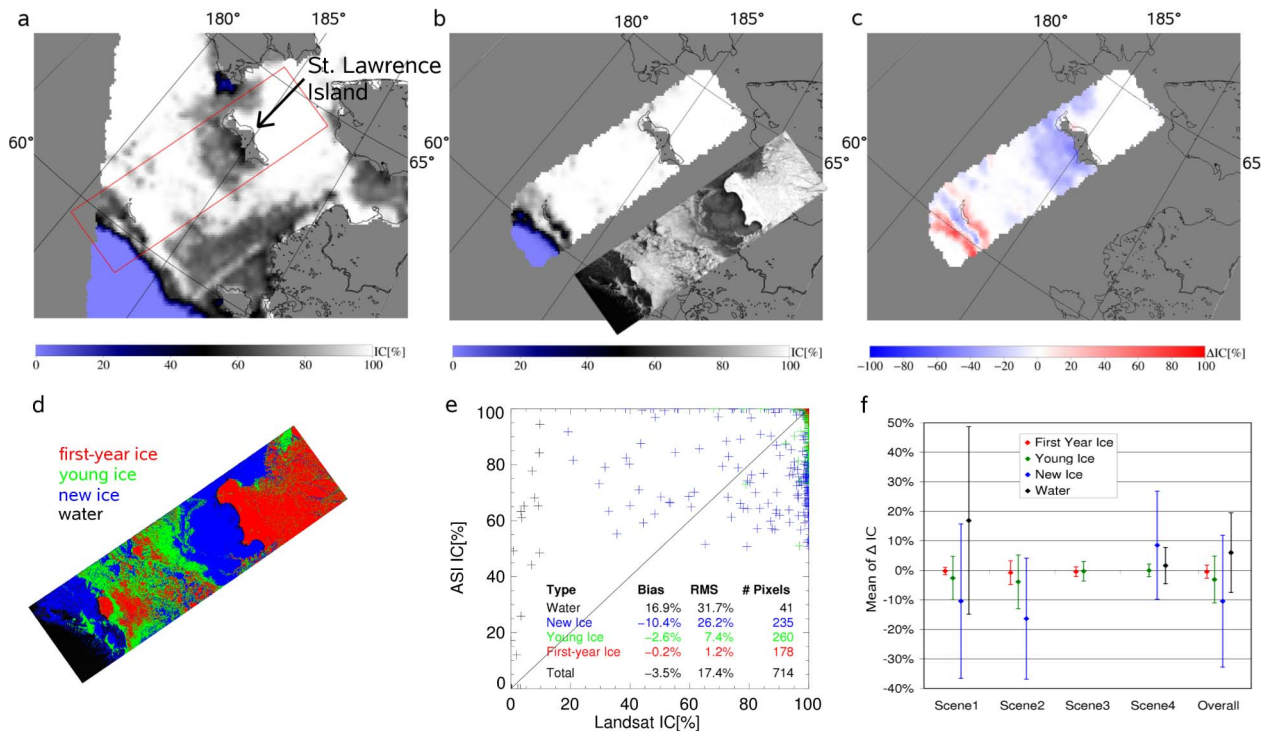|	Area [km^2]	Date	Time T [h]		$\Delta\,T$ [h]	ETM+ IC [%]		Bias [%]		RMS [%]	
			ETM+	AMSR-E		Mean	Stddev	ASI	NT2	ASI	NT2
Scene 1	192×673	2003-03-13	22:29	23:05	0:36	96.0	11.5	-3.5	-1.5	17.4	6.6
Scene 2	192×673	2003-03-15	22:16	22:52	0:36	97.6	4.1	-8.4	-1.9	14.4	6.3
Scene 3	192×184	2003-03-20	22:36	23:12	0:36	99.9	1.0	-0.4	≈ -0	2.0	1.2
Scene 4	192×184	2003-03-22	22:23	00:30	2:07	72.1	32.0	4.5	-13.8	12.8	15.8

Fig. 3. Sea-ice concentration maps of (a) ASI and (b) Landsat (with the original albedo overlay shifted to the lower right). (c) Difference map of ASI–Landsat ice concentrations. (d) Ice-type classification. (e) Scatter plot of *Scene 1* (March 13, 2003). (f) Bias (mean of Δ IC) and (error bars) rms errors of different ice types and water for all four scenes, and average values over all four scenes, weighted by the number of involved pixels.

it is 0% (only few pixels); and for new ice, it ranges from 5.1% to 8.4%.

The cross-comparison of the NT2–Landsat to the ASI–Landsat yields that, for *Scenes 1–3*, the ASI algorithm underestimates the ice concentrations up to two times stronger than the NT2 algorithm does, with the exception of *Scene 2* where ASI's bias is four times the one of NT2. The rms errors are about two to three times higher.

These results are consistent with the direct comparison of the NT2 to the ASI algorithm by Spreen *et al.* [5]. On the Northern Hemisphere, ASI underestimates the ice concentrations relative to NT2 by -2.0% with an rms error of 8.8%. The NT2 and ASI ice concentrations were computed on the AMSR-E data for the period of June 2002–August 2006 with the ASI tie points $P_0 = 47.0$ K and $P_1 = 11.7$ K, the so-called operational tie points used for the daily processed ASI sea-ice maps (see www.iup.uni-bremen.de/seaice/amsr/).

Moreover, the cross-comparison shows that NT2 detects the ice with a bias that is close to zero and lower rms errors than ASI. This is mainly due to the high errors of ASI in areas of new ice. Young ice and first-year ice have similar rms errors in both comparisons. Since NT2 uses several frequency channels for computing ice concentrations, it is able to recognize new ice more stably than ASI, which only uses the polarization difference at 89 GHz. Further discussions are given in Section III-C.

C. Discussion of Results

The ASI–Landsat comparison (Section III) shows two main issues of the ASI algorithm: It underestimates the ice concentration in polynya areas and overestimates it at the ice edge. The possible reasons of this behavior are discussed in the following paragraphs. In general, the albedo values that we consider as ground truth may also have errors, particularly regarding the anisotropic reflection of snow/ice, which can have an influence on the albedo values of 10% at solar zenith angles that are larger than 60° [14]. However, this refers essentially to higher albedo values. The important albedo threshold of 0.1 between ice and water, which is used to set the values of the Landsat pixels

to either 0% or 100% ice concentration, would only be little affected.

1) Underestimation in Polynya Areas: The underestimation of ASI ice concentrations mainly occurs in polynya areas where we have new ice. IC_{ASI} ranges between 60% and 80%, corresponding to a polarization difference P of 40–50 K according to Fig. 2. It means that new ice causes larger polarization differences than "older" ice ($P \approx 10-20$ K). Landsat generally has higher ice concentrations for new ice ($IC_{Landsat} \approx 80\%-100\%$).

A possible explanation for the lower ice concentrations of ASI in the new ice regions could be that the sea-ice temperatures of new ice are generally higher than for first-year ice. The four scenes used here have mean sea-ice temperatures on the order of 250 K for first-year ice and up to 265 K for new ice (values are from the sea-ice temperature product of MODIS). The ASI algorithm uses the polarization difference at 89 GHz. For high ice concentrations, a difference of the sea-ice temperature of ± 10 K would affect the polarization difference on the order of ± 1 K and the ice concentration of $\mp 1\%$. For low ice concentrations, a difference of the sea-ice temperature of ± 10 K would affect the polarization difference on the order of ± 2 K and the ice concentration of $\mp 4\%$. It means that lower ice concentrations and higher temperatures, which is the case for new ice, can lead to an underestimation of the ASI ice concentrations, whereas this effect is rather minor.

2) Overestimation at Ice Edge: The overestimation of the ASI ice concentrations mainly occurs at the ice edge. The ASI–Landsat comparison shows that the ice edge seems to be shifted. ASI already sees ice where Landsat still sees water. Obvious assumptions would be time gaps between the ASI and Landsat observations, and the geolocation error of AMSR-E Level 1 data. The time difference between ASI and Landsat scenes is between 0.5 and 2 h. Within this time frame, we do not expect large differences on a 12.5-km grid. From the geolocation study of AMSR-E Level 1 data [15], we know that the averaged geolocation error is 6.5 km. This, again, does not result in large changes on the 12.5-km grid. The next possible explanation for the overestimation of IC_{ASI} lies in an ice type called dark nilas. As the name indicates, it looks quite dark as it is thin and has no snow on top. Therefore, it may be seen as water in the visible range, but it is already recognized by the ASI algorithm as ice since it causes a lower polarization difference than open water. Finally, the main reason for the overestimation at the ice edge is the high tie point for water ($P_0 = 80$ K) after the ASI tie-point adaptation toward the Landsat ice concentrations. This leads to a more detailed examination of the tie points.

3) ASI Tie Points: The average ASI tie points with Landsat ice concentrations as reference are $P_0 = 80$ K and $P_1 = 20$ K, as found in Section II-D. In particular, P_0 is high compared with $P_0 = 47.0$ K, which is used in the operational ASI ice charts. From [16], we know the polarization differences P's for water and ice, measured at the surface: $P_{ice} = 10 \pm 4$ K and $P_{water} = 82 \pm 4$ K. However, the polarization difference measured by a radiometer on a satellite is lowered by the influence of the atmosphere. It means that we will not get polarization differences P's of 80 K for open water. The reason, which leads

to a tie point P_0 of 80 K, is shown in Fig. 2, showing the Landsat ice concentrations related to the polarization differences P's for all four scenes. Additionally, the third-order polynomials of the Landsat-adapted tie points (red curve) and of the operational ASI tie points (blue curve) are overlaid. Since the Landsat ice concentrations are generally rather high, the third-order polynomials tend toward high tie points in order to get higher ice concentrations in the range of 30–50 K. This leads to the effect that ASI recognizes some water pixels already as ice, resulting in the overestimation at the ice edge. With the old regression (blue curve), a polarization difference P of 47 K represents open water, while the new regression (red curve) gives an ice concentration of 65%. However, the ASI algorithm uses three weather filters in total [5], among them the bootstrap algorithm, which sets ASI pixels to 0% ice concentration wherever bootstrap has an ice concentration of 0%. When using the operational ASI tie points in contrast, there is no overestimation of ice concentrations from ASI near the ice edge, but most of the new ice is misclassified as open water. Moreover, we see that it is difficult to relate the polarization differences P's to the Landsat ice concentrations, particularly for new ice. Looking at *Scene 1* for example, we can have various ice concentrations between 10% and 100% for $P = 40$ K. As the ASI algorithm is only based on polarization differences, it is particularly hard to detect new ice. To address this problem, one could, in addition, use the lower frequency channels of AMSR-E, for instance, as the NT2 algorithm does. However, one would lose the main advantage of ASI, namely, the high spatial resolution.

IV. ICE CONCENTRATIONS DERIVED FROM SAR

A. SAR Data Set

The SAR data set used for the comparison study consists of ice concentrations derived from SAR images of Radarsat-1 (ScanSAR wide-mode data) and Envisat (wide-swath-mode data) of the Arctic, taken between May 2003 and November 2004. The sizes range between 425 km $\times$ 445 km and 560 km $\times$ 565 km. The data are gridded on a polar-stereographic grid with grid sizes of 100 m for Radarsat scenes and 75 m for Envisat scenes. The classification method of the original single-polarized SAR images is given in [8]. It is based on a supervised neural-network classification of second-order gray-level statistical features. Four different classes are distinguished: calm water, rough water, low-backscatter ice (smooth surface), and high-backscatter ice (rough surface).

Each classified SAR image comes along with a mask, which cuts out land areas and misclassified areas, such as wind-roughened sea water characterized with high-backscatter sea ice and very calm water characterized with low-backscatter ice. The method to calculate ice concentrations at 12.5-km resolution from those classified SAR pixels is as follows. In the classified SAR image, all calm- and rough-water pixels are set to 0% ice concentration, while all low- and high-backscatter ice pixels are set to 100% ice concentration. The idea of deriving heterogeneous ice concentrations from SAR is averaging the small SAR pixels over the size of the much larger ASI pixels on the polar-stereographic grid of 12.5 km. As AMSR-E cannot differentiate structures within one footprint, the distribution of

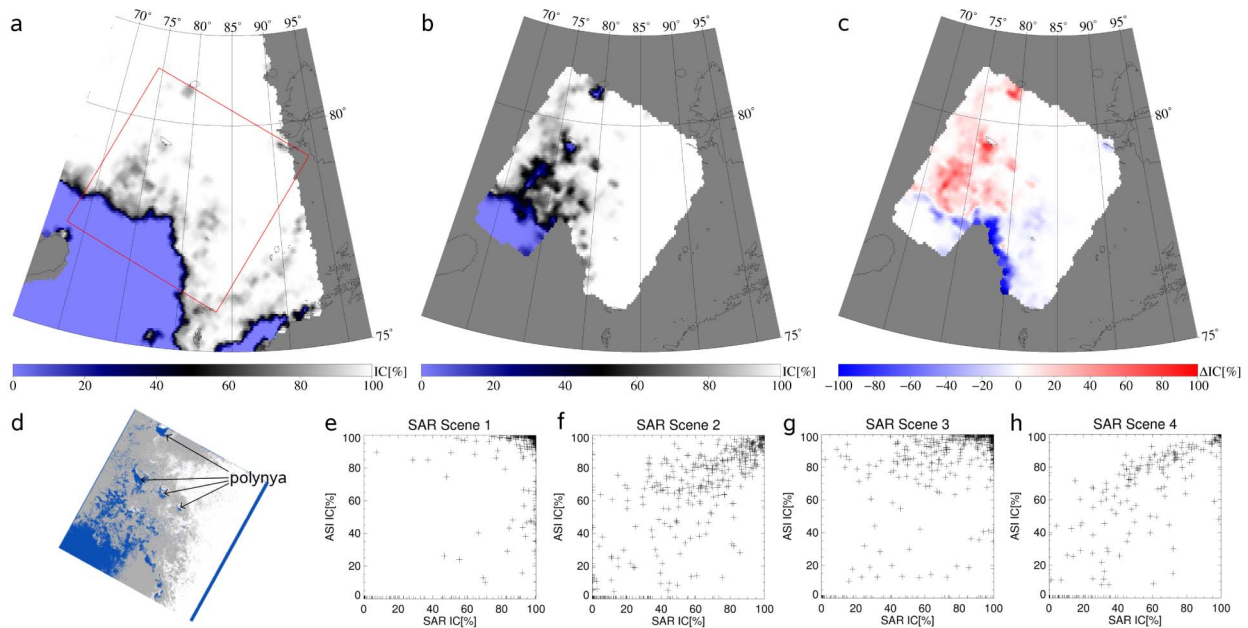|	Location	Area [km^2]	Date	Time T [h]		Δ T [h]	Bias [%]	RMS [%]	# Pixels
				SAR	AMSR-E				
Scene 1	Davis Strait	556 × 553	2004-06-21	21:10	16:22	4:48	−2.9	17.0	1110
Scene 2	Baffin Bay	559 × 565	2004-06-30	21:49	16:17	5:32	1.4	20.1	539
Scene 3	Kara Sea	431 × 445	2003-10-03	06:16	07:06	0:50	1.4	18.0	1087
Scene 4	Greenland Sea	425 × 446	2003-08-26	11:11	11:01	0:10	2.5	16.9	356

Fig. 4. Ice concentration maps of (a) ASI and (b) Envisat SAR. (c) Difference map of ASI–SAR ice concentrations. (d) Classified SAR image with classes of (light blue) calm water, (blue) rough water, (gray) low-backscatter, and (white) high-backscatter sea ice of *Scene 3* (October 3, 2003). (e)–(h) Scatter plots of all SAR scenes: ASI-versus-SAR ice concentrations.

open water and sea ice within the footprint does not matter here. As a consequence, the SAR-derived ice concentrations within each AMSR-E footprint are well defined and may be used as a reference. For the ASI ice concentrations, the same tie points as for the Landsat comparison are used (Section II-D).

B. Comparison: ASI–SAR Ice Concentrations

For the comparison of ice concentrations between ASI and SAR, four scenes are selected from a total of 39 scenes that include the ice edge. Here, we only show the images of *Scene 3*, and the other three scenes show a similar behavior. Details of all scenes are summarized in Table II. *Scenes 1* and *2* are from SAR on Radarsat-1, while *Scenes 3* and *4* are from ASAR on Envisat.

In all four SAR scenes, there are mainly cirrus clouds present, the total water vapor ranges between 5 and 10 kg/m^2, and the cloud liquid water between is well below 0.05 kg/m^2 (values are from ECMWF reanalysis data). Hence, there is only little influence on the 89-GHz channels used by ASI and practically no influence at 5 GHz used by the SAR instruments due to atmospheric conditions.

In Fig. 4(a)–(d), the results of the comparison between the ASI and SAR ice concentrations are shown. It shows maps of the ice concentrations of ASI [Fig. 4(a)] and SAR [Fig. 4(b)], their differences [Fig. 4(c)], and the classified SAR image [Fig. 4(d)]. From the difference image, we see that ASI underestimates the ice concentrations along the ice edge (blue color) and overestimates them in some interior areas (red color) with respect to the SAR ice concentrations. In the SAR image, there are small polynya areas in the wind shadow of some small islands [shown in Fig. 4(d)]. The errors mainly occur at lower ice concentrations. The biases and rms errors of all four SAR scenes are shown in Table II. The scatter plots of ASI-versus-SAR ice concentrations are shown in Fig. 4(e)–(h) for all four SAR scenes. All biases are close to 0%; they range between −2.9% and 2.6%. The rms errors are quite large, ranging from 16.9% to 20.1%.

In addition to the ASI–SAR comparison, we looked at how the ice concentration from NT2 compares to the ice concentration from SAR for the same SAR scenes (figures not shown here). In principle, ASI–SAR and NT2–SAR show similar features. NT2 underestimates the ice concentrations compared to SAR in areas where ASI does and overestimates them where ASI does. Particularly at the ice edge, NT2 underestimates

SAR less than ASI does. However, in some interior areas, NT2 underestimates the ice concentrations where the ASI and SAR ice concentrations are in good agreement. In total, the bias of the NT2–SAR comparison is on the order of 5% lower than the bias of the ASI–SAR comparison.

V. LIMITATIONS OF THE THREE SENSOR TYPES REGARDING THIN ICE

The comparisons of ASI–Landsat and ASI–SAR ice concentrations show that the largest differences occur for the new ice, whereas the results are contradictory. At the ice edge, ASI overestimates the ice concentrations compared to Landsat and underestimates it compared to SAR, and for some areas, in the ice interior, it is vice versa. Therefore, we want to consider the interaction mechanisms of the different sensor types (optical, active, and passive microwaves) with new/thin ice.

In the optical range, the albedo of snow-free sea ice increases monotonically with thickness during ice growth; Weller [17] measured albedos of 0.08 for open water, which increased to 0.40 for 30-cm-thick ice. Thus, the albedo is a good quantity to distinguish open water and ice. However, the ice-type dark nilas, which forms under calm conditions, has an albedo that is similar to that of open water [18]–[20].

Active microwave sensors are suitable for detecting the ice edge, whereas ice concentrations are rather difficult to estimate, particularly in areas of new ice. The measured quantity of an active microwave sensor, the backscatter intensity, detects the roughness of the surface. Since both open water and sea-ice surface can be either rough (wind-roughened sea water—pancake ice) or smooth (calm water—nilas), it is sometimes difficult to distinguish between them. In the initial stage of ice growth, the backscatter intensity reduces as the ice crystals (grease) on the water smooth the surface and as the dielectric constant decreases due to brine rejection. In the next stage of ice growth, nilas (smooth surface) cause lower backscatter, while pancake ice or frost flowers on nilas (rough surface) cause higher backscatter. It means that the new ice has a broad range of backscatter intensities [21]–[23].

Passive microwave sensors show a rather monotonic increase in brightness temperature during ice formation, and even more importantly, the difference between vertically and horizontally polarized radiation decreases, whereas it remains constant for open water. Ice and open water can therefore be distinguished reliably. The polarization difference of thin ice is similarly high as that of open water, particularly near 90 GHz, as used by the ASI algorithm. Therefore, areas of thin ice are frequently mistaken for areas of low ice concentrations. Other sea-ice algorithms that use lower frequencies (19 and 37 GHz) may be able to better detect thinner ice types [2], [24], [25].

VI. SUMMARY AND CONCLUSION

The differences of the ASI ice concentrations compared to the four visual Landsat-7 ETM+ scenes vary with the ice type. First-year ice (bias: -0.2% to -0.8% and rms: 1.2%–4.0%) and young ice (bias: -0.3% to -3.9% and rms: 9.1%–3.3%) are well recognized by the ASI algorithm.

The values are similar if compared to the results of the NT2–Landsat comparison, which had biases for first-year ice from -0.4% to -3.5% and rms errors from 1.2% to 4.7% (Section III-B). New ice is recognized with less reliability. It mainly occurs at the ice edge and in polynya areas. It causes a bias of -16.4%–8.5% and an rms error of 18.3%–26.2%. Summarized over all ice types and water, we have biases of -8.4%–4.5% and rms errors of 2.0%–17.4%. The errors along the ice edge cannot be attributed to time shift or geolocation error. They are mainly caused by the high tie point $P_0 = 80$ K. However, with the lower tie point $P_0 = 47.0$ K, most of the new ice is recognized as water. The errors in the polynya areas are due to the fact that new ice causes a broad range of polarization differences, making it difficult to exactly map from polarization difference to ice concentration (Fig. 2).

The comparison of ASI ice concentrations with those derived from SAR yields in a certain sense opposite results to the ASI–Landsat comparison. Relative to SAR, ASI underestimates the ice concentrations near the ice edge and overestimates them in some interior areas (presumably polynyas). The biases of the four scenes used in the ASI–SAR comparison lie between -2.9% and 2.5%. The rms errors show a scatter between 16.9% and 20.1%.

The contrasting results of the comparisons of ASI with Landsat and SAR show that the data considered as ground truth (Landsat and SAR data) may detect different ice types differently as the sensor types have fundamentally different physical interaction mechanisms with sea ice, specifically for new and thin ice with a thickness up to roughly 30 cm. For all three sensor types used here, thin ice often does not have a very distinct difference to open water, which may lead to misinterpretations (see Section V).

The discrepancies emerging in the comparisons of ASI–Landsat and ASI–SAR ice concentrations may also be caused from the different dates of the Landsat and SAR data. In the ASI–Landsat comparison, all scenes are taken during winter freezing conditions, while in the ASI–SAR comparison, they are taken during summer melting conditions. It means that there are different interaction mechanisms due to not only different sensor types but also different sea-ice conditions. However, the ranges of biases of the ASI ice concentrations are quite good in both comparisons, whereas the rms errors are rather high. The fast delivery and higher horizontal resolution, compared to other ice concentration products based on passive microwave data, make the ASI data attractive for ship navigation and operational applications when sea-ice concentrations in near real time and at good horizontal resolution are required. For climate studies, e.g., as input for climate models, a tradeoff between horizontal resolution and precision in ice concentration has to be met because data of lower error in ice concentration but coarser spatial resolution are also available.

REFERENCES

[1] D. J. Cavalieri, P. Gloersen, and W. J. Campbell, "Determination of sea ice parameters with the NIMBUS-7 SMMR," *J. Geophys. Res.*, vol. 89, no. D4, pp. 5355–5369, 1984.

[2] D. J. Cavalieri, "A microwave technique for mapping thin sea ice," *J. Geophys. Res.*, vol. 99, no. C6, pp. 12 561–12 572, 1994.

[3] J. C. Comiso, "Characteristics of Arctic winter sea ice from satellite multispectral microwave observations," *J. Geophys. Res.*, vol. 91, no. C1, pp. 975–995, 1986.

[4] J. C. Comiso, "SSM/I sea ice concentrations using the bootstrap algorithm," NASA, Goddard Space Flight Center, Greenbelt, MD, NASA Ref. Pub., 1380, 1995. 49 pp.

[5] G. Spreen, L. Kaleschke, and G. Heygster, "Sea ice remote sensing using AMSR-E 89-GHz channels," *J. Geophys. Res.*, vol. 113, no. C2, p. C02 S03, 2008.

[6] D. J. Cavalieri, T. Markus, D. K. Hall, A. Gasiewski, M. Klein, and A. Ivanoff, "Assessment of EOS Aqua AMSR-E Arctic sea ice concentrations using Landsat-7 and airborne microwave imagery," *IEEE Trans. Geosci. Remote Sens.*, vol. 44, no. 11, pp. 3057–3069, Nov. 2006.

[7] T. Markus and D. J. Cavalieri, "An enhancement of the NASA Team sea ice algorithm," *IEEE Trans. Geosci. Remote Sens.*, vol. 38, no. 3, pp. 1387–1398, May 2000.

[8] T. Bøvith and S. Andersen, "Sea ice concentration from single-polarized SAR data using second-order grey level statistics and learning vector quantization," Danish Meteorol. Inst., Copenhagen, Denmark, 2005. Tech. Rep.

[9] G. Chander and B. Markham, "Revised Landsat-5 TM radiometric calibration procedures and postcalibration dynamic ranges," *IEEE Trans. Geosci. Remote Sens.*, vol. 41, no. 11, pp. 2674–2677, Nov. 2003.

[10] L. Kaleschke, "Fernerkundung des Meereises mit passiven und aktiven Mikrowellensensoren," Ph.D. dissertation, Inst. Environ. Phys., Univ. Bremen, Bremen, Germany, 2003. 192 pp.

[11] J. A. Nelder and R. Mead, "A simplex method for function minimization," *Comput. J.*, vol. 7, no. 4, pp. 308–313, 1965.

[12] O. Arino, E. Vermote, and V. Spaventa, "Operational atmospheric correction of Landsat TM imagery," *ESA Earth Obs. Q.*, vol. 56, pp. 32–35, 1998.

[13] R. Drucker, S. Martin, and R. Moritz, "Observations of ice thickness and frazil ice in the St. Lawrence Island polynya from satellite imagery, upward looking sonar, and salinity/temperature moorings," *J. Geophys. Res.*, vol. 108, no. C5, p. 3149, 2003.

[14] T. H. Painter and J. Dozier, "The effect of anisotropic reflectance on imaging spectroscopy of snow properties," *Remote Sens. Environ.*, vol. 89, no. 4, pp. 409–422, Feb. 2004.

[15] H. Wiebe, "Validation of the ARTIST Sea Ice (ASI) concentration algorithm and geolocation of the microwave radiometer AMSR-E data," M.S. thesis, Inst. Environ. Phys., Univ. Bremen, Bremen, Germany, 2007. 82 pp.

[16] E. Svendsen, C. Mätzler, and T. C. Grenfell, "A model for retrieving total sea ice concentration from a spaceborne dual-polarized passive microwave instrument operating near 90 GHz," *Int. J. Remote Sens.*, vol. 8, no. 10, pp. 1479–1487, Oct. 1987.

[17] G. Weller, "Radiation flux investigations," *AIDJEX Bull.*, vol. 14, pp. 28–30, 1972.

[18] D. K. Perovich, "The optical properties of sea ice," U.S. Army Cold Reg. Res. Eng. Lab., Hanover, NH, 1996. Monogr. 96-1, 25 pp.

[19] K. C. Jezek, D. K. Perovich, K. M. Golden, C. Luther, D. G. Barber, P. Gogineni, T. C. Grenfell, A. K. Jordan, C. D. Mobley, S. V. Nghiem, and R. G. Onstott, "A broad spectral, interdisciplinary investigation of the electromagnetic properties of sea ice," *IEEE Trans. Geosci. Remote Sens.*, vol. 36, no. 5, pp. 1633–1641, Sep. 1998.

[20] T. C. Grenfell, D. G. Barber, A. K. Fung, A. J. Gow, K. C. Jezek, E. J. Knapp, S. V. Nghiem, R. G. Onstott, D. K. Perovich, C. S. Roesler, C. T. Swift, and F. Tanis, "Evolution of electromagnetic signatures of sea ice from initial formation to the establishment of thick first-year ice," *IEEE Trans. Geosci. Remote Sens.*, vol. 36, no. 5, pp. 1642–1654, Sep. 1998.

[21] R. G. Onstott, "SAR and scatterometer signatures of sea ice," in *Microwave Remote Sensing of Sea Ice*, ser. Geophysical Monograph Series, vol. 68, F. D. Carsey, Ed. Washington, DC: Amer. Geophys. Union, 1992, pp. 73–104.

[22] R. Kwok, S. V. Nghiem, S. Martin, D. P. Winebrenner, A. J. Gow, D. K. Perovich, C. T. Swift, D. G. Barber, K. M. Golden, and E. J. Knapp, "Laboratory measurements of sea ice: Connections to microwave remote sensing," *IEEE Trans. Geosci. Remote Sens.*, vol. 36, no. 5, pp. 1716–1730, Sep. 1998.

[23] L. M. H. Ulander, A. Carlström, and J. Askne, "Effect of frost flowers, rough saline snow and slush on the ERS-1 SAR backscatter of thin Arctic sea-ice," *Int. J. Remote Sens.*, vol. 16, no. 17, pp. 3287–3305, 1995.

[24] M. Wensnahan, G. A. Maykut, and T. C. Grenfell, "Passive microwave remote sensing of thin sea ice using principal component analysis," *J. Geophys. Res.*, vol. 98, no. C7, pp. 12 453–12 468, 1993.

[25] T. Markus and B. A. Burns, "A method to estimate subpixel-scale coastal polynyas with satellite passive microwave data," *J. Geophys. Res.*, vol. 100, no. C3, pp. 4473–4487, 1995.

Heidrun Wiebe received the B.S. degree in information technology from the University of Cooperative Education, Mannheim, Germany, in 2003 and the M.S. degree in environmental physics from the University of Bremen, Bremen, Germany, in 2007, where she is currently working toward the Ph.D. degree in the Institute of Environmental Physics.

Her research interests include satellite remote sensing of arctic regions.

Georg Heygster (M'00) received the Diploma degree in solid state physics and the Ph.D. degree in digital image processing from the University of Göttingen, Göttingen, Germany, in 1976 and 1979, respectively.

He was a Consultant with the Computer Center, University of Bremen, Bremen, Germany, from 1979 to 1988. Since then, after one year working on the imaging mechanisms of scanning acoustic microscopes, he has been the Head of the Geophysical Analysis of Satellite Images Group, Institute of Environmental Physics, University of Bremen. He has been the Principal Investigator or a Coinvestigator of many research projects funded by the European Union, the European Space Agency, the Deutsche Forschungsgemeinschaft, and the Japan Aerospace Exploration Agency. These projects include the development of sensor software and hardware, conducting campaigns, the final data analysis from multi- and single-sensor data to geophysical parameters, and the interpretation and application of these results in many areas such as meteorology, climatology, and oceanography. His research activities include passive and active microwave remote sensing, particularly of both surface and atmospheric parameters in high latitudes, various aspects of the hydrological cycle, long-term trends, and retrieval techniques.

Thorsten Markus (M'05) received the M.S. and Ph.D. degrees in physics from the University of Bremen, Bremen, Germany, in 1992 and 1995, respectively.

He is currently a Research Scientist with the NASA Goddard Space Flight Center (GSFC), Greenbelt, MD. From 1995 to 1996, he was a National Research Council Resident Research Associate with GSFC before joining the NASA–UMBC Joint Center for Earth Systems Technology, where he worked until 2002. His research interests include satellite microwave remote sensing of primarily ice and the utilization of satellite data to study oceanic and atmospheric processes.

Dr. Markus is a member of the American Geophysical Union.